Spiral-like holographic structures: Unwinding interference carpets of Coulomb-distorted orbits in strong-field ionization

Andrew S. Maxwell* and Carla Figueira de Morisson Faria
Department of Physics and Astronomy, University College London, Gower Street, London, WC1E 6BT, United Kingdom

XuanYang Lai, RenPing Sun, and XiaoJun Liu
State Key Laboratory of Magnetic Resonance and Atomic and Molecular Physics, Wuhan Institute of Physics and Mathematics, Innovation Academy for Precision Measurement Science and Technology, Chinese Academy of Sciences, Wuhan 430071, China

(Received 4 March 2020; revised 17 August 2020; accepted 28 August 2020; published 21 September 2020)

We unambiguously identify, in experiment and theory, an overlooked holographic interference pattern in strong-field ionization, dubbed "the spiral," stemming from two trajectories where the potential and laser field are equally critical. Because of the strong interaction with the core of the two trajectories, the spiral could be employed as an optimal tool for probing the target *after* ionization and for revealing obfuscated phases in the bound states. We find that the spiral is responsible for interference carpets, formerly ascribed to direct trajectories, and that the carpet-interference condition is derived from the field symmetry. This case of mistaken identity may have prevented the spiral from being used as a holographic tool.

DOI: 10.1103/PhysRevA.102.033111

I. INTRODUCTION

Matter in intense laser fields ($I = 10^{13}\,\mathrm{W/cm^2}$ or higher) has led to the inception of attoscience. Attoseconds are some of the shortest timescales in nature, which allows real-time probing of electron dynamics and, potentially, target reconstruction [1–9]. In order to reconstruct targets, one must measure both amplitudes and phase differences. This requirement has caused the development of ultrafast photoelectron holography [10–13], exploiting the quantum interference of different paths that an electron can take during strong-field ionization to produce a holographic image, which includes the phase information. Typically, there is a direct (*reference*) pathway and one that reinteracts with the target (*probe*). Phases imprinting structural information are acquired when the probe returns close to the parent ion. Hence, for optimal imaging one should minimize the closest distance from the core upon return. Examples of holographic patterns are spider-like [12,14], fan-shaped [15,16], and fish-bone-type fringes [17].

The fan and the spider result from the interference of direct trajectories [18,19] and two types of forward-scattered trajectories [12,14,19], respectively. Despite a brief interaction with the core, they can still be used to probe the target. Enhancements in the fan were related to electron-nuclear coupling in H_2 [20], while the spider has been shown to be sensitive to molecular orientation [21] and the dynamics of nodal planes [22]. Still, the above-stated effects either relate to the structureless Coulomb tail or to phase differences obtained *prior* to ionization in the target's initial bound states. Nonetheless, there is a strong motivation to image changes that happen subsequently to ionization, such as polarization, charge migration, or multielectron dynamics. Thus, a stronger interaction with the core during continuum propagation is desirable. The fish-bone structure reported in Ref. [17] is associated with backscattered trajectories but was obfuscated by the spider-like fringes, which made an elaborate scheme necessary in order to retrieve the structure.

Instead, one may seek holographic structures in regions where the spider is suppressed, such as for final momenta perpendicular to the laser-field polarization. Interference carpets occur in such a region [23–31], but were attributed to direct strong-field approximation (SFA) orbits and their interplay with above-threshold ionization (ATI) rings [23,24]. However, this interpretation is debatable. First, the energy region for which they are observed is much higher than the direct ATI $2U_p$ cutoff, where U_p is the ponderomotive energy [32]. Second, a theoretical study [27] concluded that the Coulomb tail enhanced forward-scattered trajectory yields in carpet-like interferences. This invites the question of why rescattering is not important for interference carpets.

We show that the above explanation for the carpet-like structure is incomplete. In the high-energy photoelectron region, we find a spiral-like pattern resulting from the interference between Coulomb-distorted back- and forward-scattered electron trajectories, which is responsible for the carpet-like structure and could be used as a holographic tool. This spiral-like pattern is clearly visible in our experiments.

The orbits causing the spiral have no counterpart in the SFA, either direct or rescattered. SFA-like approaches are Born-type series which establish artificial boundaries between "direct" and "rescattered" orbits and exclude those in between [33]. There are, however, orbit-based methods that incorporate the residual potential and the driving field on an equal footing [13]. One such method, used

*andrew.maxwell@ucl.ac.uk

in this work, is the Coulomb quantum orbit strong-field approximation (CQSFA).

This article is organized as follows. In Sec. II, we provide a brief account of the theoretical (II A) and experimental (II B) methods used in this work. Subsequently, in Sec. III, we discuss our results with regard to the structure itself (III A), its phase sensitivity (III B), and its universality (III C). Our conclusions are stated in Sec. IV.

II. BACKGROUND AND METHODS

A. Coulomb quantum-orbit strong-field approximation

The CQSFA enables an incredibly clear picture of quantum interference that has revealed a whole host of previously overlooked patterns [18,19,33–35]. It employs the exact transition amplitude for single-electron strong field ionization [36]:

$$M(\mathbf{p}) = -i \lim_{t\to\infty} \int_{-\infty}^{t} dt' \langle \psi_{\mathbf{p}}(t)|\hat{U}(t,t')H_I(t')|\Psi_0(t')\rangle, \quad (1)$$

where $|\Psi_0(t')\rangle = e^{iI_p t'}|\Psi_0\rangle$ is the initial state and $|\psi_{\mathbf{p}_f}(t)\rangle$ is a final plane-wave state with momentum $\mathbf{p}_f$. The time evolution operator $\hat{U}(t,t')$ relates to the full Hamiltonian $\hat{H}(t) = \hat{\mathbf{p}}^2/2 + V(\hat{\mathbf{r}}) + \hat{H}_I(t)$, where $V(\hat{\mathbf{r}})$ is the binding potential and $\hat{H}_I(t) = \hat{\mathbf{r}}\cdot\mathbf{E}(t)$ is the interaction with the field. Using a path-integral formalism and the saddle-point approximation, this becomes the sum

$$M(\mathbf{p}_f) \propto -i \lim_{t\to\infty} \sum_s \left\{ \det\left[\frac{\partial \mathbf{p}_s(t)}{\partial \mathbf{r}_s(t_s)}\right]\right\}^{-1/2} \mathcal{C}(t_s) e^{iS(\mathbf{p}_s,\mathbf{r}_s,t,t_s)} \quad (2)$$

over s quantum orbits. The action along each orbit reads

$$S(\mathbf{p},\mathbf{r},t,t') = I_p t' - \int_{t'}^{t} [\dot{\mathbf{p}}(\tau)\cdot\mathbf{r}(\tau) + H(\mathbf{r}(\tau),\mathbf{p}(\tau),\tau)]d\tau, \quad (3)$$

where the momentum $\mathbf{p}$ and coordinate $\mathbf{r}$ have been parametrized in terms of the time τ. The integral in Eq. (3) diverges at the lower bound; this is fixed using a regularization procedure [37–39]. The variables t_s, $\mathbf{p}_s$, and $\mathbf{r}_s$ are determined by the saddle-point equations

$$[\mathbf{p}(t') + \mathbf{A}(t')]^2/2 + I_p = 0, \quad (4)$$

$$\dot{\mathbf{p}}(\tau) = -\nabla_{\mathbf{r}} V[\mathbf{r}(\tau)] \quad \text{and} \quad \dot{\mathbf{r}}(\tau) = \mathbf{p}(\tau) + \mathbf{A}(\tau), \quad (5)$$

and $\mathcal{C}(t_s)$ is given by

$$\mathcal{C}(t_s) = \sqrt{\frac{2\pi i}{\partial^2 S(\mathbf{p}_s,\mathbf{r}_s,t,t_s)/\partial t_s^2}}\, \langle \mathbf{p} + \mathbf{A}(t_s)|H_I(t_s)|\Psi_0\rangle, \quad (6)$$

where $|\Psi_0\rangle$ refers to the initial electronic bound state of the electron, computed with GAMESS-UK [40] for xenon, neon, and helium. We use a monochromatic field throughout in the CQSFA simulations. This is a widely used approximation for sufficiently long pulses [41], for which the field cycles will be practically identical. In this long-pulse regime, increasing the number of cycles will increase the contrast of the interference patterns but will not alter their energy position. For that reason, monochromatic waves or combinations thereof have been extensively used in previous SFA computations in comparison with experiments and *ab initio* simulations [23,24,42,43]. In practice, the ionization times t' are restricted to a finite range, with an arbitrary unit cell. This choice may lead to an offset phase, which may lead to a certain asymmetry with regard to the $p_\perp$ axis for a single cycle. This offset will vanish as the ionization time range is increased. Unless otherwise stated (see, e.g., Fig. 1), we employ a four-cycle range for t'. The CQSFA, in its implementation, is propagated for a finite time t, and thus care must be taken regarding the use of a final plane wave momentum state; see Refs. [44,45] for details. For the propagation times used in this work, we estimate that for an electron with a final momentum below $|\mathbf{p}_f| = 0.2$ a.u. ($E = 0.54$ eV) some differences may be present compared to if we employed exact scattering states. These low-energy electrons do not make it into the so-called asymptotic regime, where this approximation is considered valid [45]. In this work, we do not focus on the low-energy electrons.

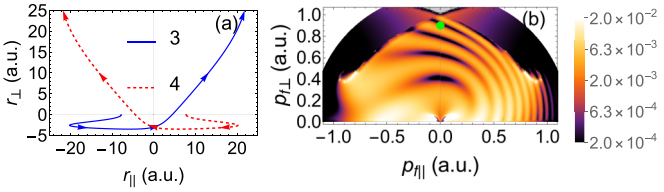

FIG. 1. (a) Example trajectories for orbits 3 and 4 with final momentum components marked by green spot at the top of panel (b). (b) Spiral-like interference in the photoelectron momentum distribution computed using the CQSFA for a laser intensity $I = 7\times10^{13}$ W/cm^2 and wavelength of 800 nm over a single cycle for a xenon target with $I_p = 0.446$ a.u.

In contrast to previous calculations [18,33–35,37,46],[1] here we employ the single-electron effective potential [47,48]

$$V(\mathbf{r}(\tau)) = -\frac{1 + f(r(\tau))}{r(\tau)}, \quad (7)$$

where $f(r) = a_1 e^{-a_2 r} + a_3 r e^{-a_4 r} + a_5 e^{-a_6 r}$ and $r(\tau) = \sqrt{\mathbf{r}(\tau)\cdot\mathbf{r}(\tau)}$, and the a_i values used are listed in Table I. We will denote hydrogenic and xenon potentials as V_H and V_{Xe}, respectively. Similar to previous work [19], one may simplify the action using

$$\dot{\mathbf{p}}(\tau)\cdot\mathbf{r}(\tau) = V(\mathbf{r}(\tau)) - f'(r(\tau)). \quad (8)$$

The four orbits are classified as in Ref. [49]. In orbit 1 (direct), the electron tunnels toward the detector and reaches it directly. In orbit 2 (forward deflected) and orbit 3 (forward scattered), the electron tunnels away from the detector and then turns around to reach the detector. For orbit 3, the electron's transverse momentum changes sign, while for orbit 2 it does not. In orbit 4 (backscattered), the electron is freed toward the detector but backscatters off the core. For details, see our previous work [33] and the review [13]. One should note that orbit 3 has no counterpart in the SFA, and is present only in Coulomb-distorted approaches that treat the potential

[1]For the tunneling step, the species is already fully accounted for and thus an effective potential is not required.

TABLE I. The a_i parameters for the single-electron effective potential for noble gases. Values for xenon are used in Figs. 2–3 and those for helium and neon in Fig. 5. Values taken from Refs. [47,48]. For hydrogen $a_i = 0\ \forall\ i$.

Atom	a_1	a_2	a_3	a_4	a_5	a_6
Helium	1.231	0.662	−1.325	1.236	−0.231	0.480
Neon	8.069	2.148	−3.570	1.986	0.931	0.602
Xenon	51.356	2.112	−99.927	3.737	1.644	0.431

and the field on equal footing (see, e.g., Refs. [34,49] for details).

In Fig. 1(a), we show the CQSFA orbits 3 and 4, whose interference gives spiral-shaped fringes, shown in Fig. 1(b) [33]. The spiral-shaped fringes are most clearly observed in the high-energy part of the distribution close to the perpendicular momentum axis. For clarity, we have considered a unit cell within a single cycle of the field. This is a precaution in order to exclude the above-threshold ionization (ATI) rings, which are typically quite prominent, and single out the spiral. The asymmetry is due to the choice of the unit cell within a field cycle, which were chosen in order to render both orbits continuous and to best display the features in the spiral.

B. Experimental setup

In the experiment, we employed a commercial laser system (FEMTOPOWER Compact PRO, Femtolasers Produktions GmbH) with a broadband femtosecond oscillator and a multipass chirped-pulse amplifier. The system delivered 30-fs pulses (FWHM) with a maximal output energy of 0.8 mJ, a central wavelength of 800 nm, and a repetition rate of 5 kHz. The pulse energy from the amplifier was adjusted by means of a broadband achromatic half-wave plate followed by a thin-film polarizer. The linearly polarized pulses were focused into the interaction chamber by an on-axis spherical mirror with a focal length of 75 mm. The gas was fed into the interaction chamber through a needle valve. The ejected electrons were detected using a velocity map imaging (VMI) spectrometer [50]. Images were recorded using a delay-line position-sensitive detector. Retrieval of the velocity and angular distribution of the measured photoelectrons was performed by using the Gaussian basis-set expansion Abel transform method [51]. The pulse length was determined to be of 11 cycles, which is enough to render the cycles approximately identical and carrier-envelope phases (CEP) effects irrelevant. Hence, the monochromatic wave in Sec. II A is a good approximation.

III. RESULTS AND DISCUSSION

A. The spiral in experiment

In Fig. 2(a), we show experimental results for strong-field ionization of xenon compared with CQSFA computations [Figs. 2(b) and 2(c) and Figs. 3(a) and 3(b)]. Figure 2 is plotted over the photoelectron emission angle (θ) and energy (E) in order to distinguish the spiral (V shape) from ATI rings (horizontal lines). There is excellent agreement between the experiment and the CQSFA, Figs. 2(a) and 2(b), respectively, aside from a slight shift of 0.7 eV, which can be explained by polarizability of xenon [54]. In the high-energy region around $\theta \approx 90^\circ$, the V-shaped (spiral) and the horizontal (ATI rings) fringes combine to make oval shapes. In Fig. 3(b), the contributions of orbits 3 and 4 are plotted. Both the V-shaped structure and ovals are reproduced in the energy region of interest. If orbit 4 is removed, the carpet-like structure disappears [Fig. 2(c)], clearly illustrating the importance of orbit 4 in the high-energy region. Hence, the spiral is unambiguously identified as the cause of these high-energy fringes. The combination of the spiral-like structure and ATI rings in this energy region leads to the interference carpets. In the lower energy regions, our results show that other CQSFA orbits start to play a role in the interference carpets at and away from the $\theta = 90^\circ$ axis. Thus, in that region, the carpets result from the interference of several types of orbits and the explanation in terms of orbits 1 and 2 is not sufficient.

One of the main features is that, along the line $\theta = 90^\circ$, there is a spacing of 2ω between the ovals (see Fig. 2) obeying

$$I_p + U_p + E_k = 2n\omega, \tag{9}$$

where n is an integer and $E_k = 1/2p_\perp^2$ is the electron's kinetic energy [23,24]. This gap stems from the mirror symmetry

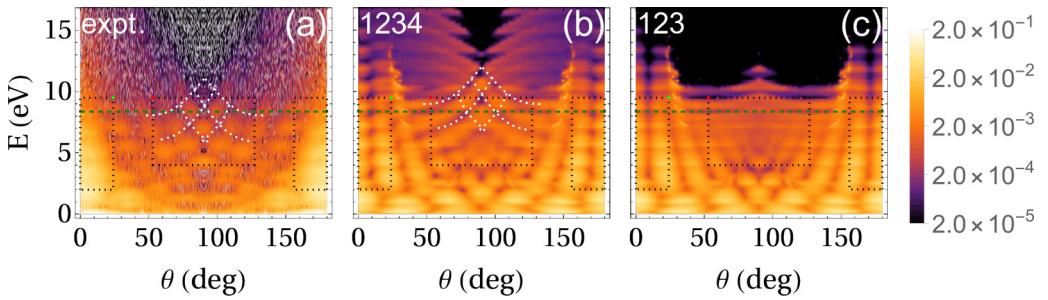

FIG. 2. Photoelectron signal for ATI of xenon. (a) Experimental data using an 11-cycle pulse of peak intensity $I = 7 \times 10^{13}\,\mathrm{W/cm^2}$ and wavelength $\lambda = 800$ nm ($\omega \approx 1.55$ eV). Theory employing the CQSFA for the same parameters but over four laser cycles. Panel (b) includes all orbits, and panel (c) includes all orbits except orbit 4. All theoretical results are focally averaged [52]. The spiral-like fringes in panel (a) are traced by white dotted lines and superimposed over panel (b). The $2U_p$ cutoff is marked by a green dashed line. The central (outer) dotted rectangle(s) mark the region where the spiral (spider) is dominant. A logarithmic scale is used over four orders of magnitude. The scale is in arbitrary units and normalized by the peak value in each panel.

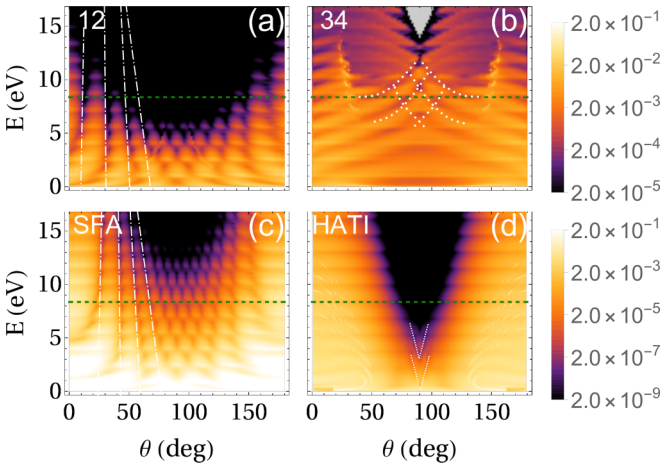

FIG. 3. Photoelectron signal for ATI of xenon computed using the CQSFA [(a), (b)] and SFA [(c), (d)]. The same target and field parameters were used as in Fig. 2. Panel (a) includes only orbits 1 and 2; panel (b) includes only orbits 3 and 4. (c) Theoretical results using the direct SFA orbits [24]. (d) Signal computed using high-order rescattered ATI (HATI) (see Refs. [33,53]). The HATI prefactors have been neglected. All theoretical results are focally averaged [52]. The spiral-like fringes are traced by white dotted lines in panel (b). The $2U_p$ cutoff is marked by a green dashed line. A logarithmic scale is used over four and eight orders of magnitude for panels (a) and (b) and panels (c) and (d), respectively. The scale is in arbitrary units and normalized by the peak value in each panel.

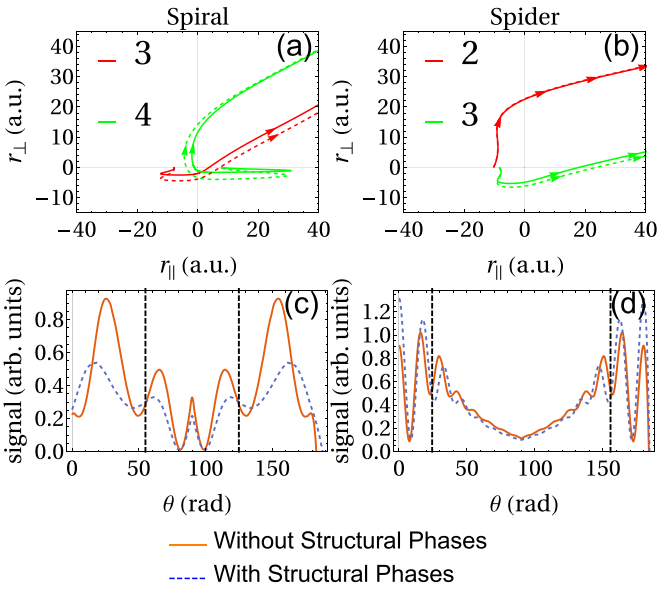

FIG. 4. Top row: Trajectories responsible for spiral (a) and spider (b) for the same target (xenon) and field parameters as Fig. 2, with a final energy $E = 9.5$ eV and angles $\theta = 53^\circ$ and $\theta = 24^\circ$ for panels (a) and (b), respectively. Solid lines [dashed lines] computed with the V_H [V_{Xe}] potential. Bottom row: CQSFA photoelectron signal for spiral (c) and spider (d) for an energy $E = 9.5$ eV. Orange lines [blue dashed lines] consider V_H [V_{Xe}] in the continuum. Inside [outside] the vertical black dashed line is the region where the spiral [spider] is dominant; see Fig. 2.

about the $r_\perp$ axis for pairs of interfering trajectories separated by exactly one half cycle, which leads to almost all phases canceling out, including those related to the Coulomb potential. In Appendix A, we show analytically that Eq. (9) is universal and is satisfied by pairs of direct and rescattered (high-order) ATI (HATI) SFA orbits and CQSFA trajectories. Equation (9) is due to a fundamental symmetry present for linear monochromatic fields and can be framed as a dipole selection rule. Demonstrating that a model satisfies Eq. (9) is not sufficient evidence of the physical mechanism for the carpet.

There are fundamental discrepancies for the carpet-like structure between the present CQSFA interpretation and the direct SFA previously given in Refs. [23,24] [see Fig. 2(b) vs Fig. 3(c)], namely, (1) the signal associated with direct orbits is very low in the region of interest, while the contributions of orbits 3 and 4 dominate, and (2) although the carpet structure is reproduced at exactly $\theta = 90^\circ$, away from this the interference of direct SFA orbits lead to sharp V-shaped fringes, for which there is significant disagreement with experiment [Fig. 2(a)]. If one uses CQSFA orbits 1 and 2 [Fig. 3(a)], the fringes are slightly straighter and fan-like [19,34], worsening the agreement with experiment. In Fig. 3(d), we plot contributions from two pairs of high-order above-threshold ionization (HATI) orbits [55], computed using the SFA, with ionization times separated by half a cycle. The HATI SFA trajectories neglect the Coulomb interaction except for a single rescattering event at the origin. In this case, there is almost no signal in the region of interest and the interference washes out very rapidly away from $\theta = 90^\circ$. It should be noted that this is only one pair out of many possible HATI quantum orbits, including some forward-scattered trajectories which contribute to high energies for 90 deg [56–58]. However, it is unclear whether interference of these quantum orbits could replicate the spiral-like interference pattern. Because the CQSFA and the SFA with rescattering are structurally different, there is not a one-to-one correspondence of the orbits in both models. For details, see our previous publication [33]. An exhaustive search through all the HATI quantum orbits is beyond the scope of this work. Thus, the direct SFA fails to replicate the interference carpet, while it is uncertain if HATI quantum orbits could do so. In contrast, the use of orbits 3 and 4 in our work are found to qualitatively well reproduce the spiral structure.

B. Sensitivity of the spiral-like structure

Three reasons make the spiral an ideal candidate for extracting information about the residual core via electron holography. First, it is visible without any additional manipulation because in the angle-energy region of interest only electron orbits 3 and 4 are dominant. Second, for $\theta = 90^\circ$, phase differences that are usually hidden can be extracted [46]. Third, these two trajectories revisit the ion core very closely, undergoing strong interaction with the binding potential.

In Figs. 4(a) and 4(b), the orbits for the spiral and spider are plotted. To demonstrate the large Coulomb interaction in the spiral orbits upon the electron's return, we compare the effect of replacing V_{Xe} for V_H in the dynamics and Coulomb phase. For the spiral, the orbits follow noticeably different paths if V_H or V_{Xe} is used, while for the spider this difference is small. The

TABLE II. Comparison of the spiral and spider patterns sensitivity to atomic structure. The second column shows the closet point of the trajectories given by r_c. Column 3 gives the ratio of the effective potential $V_{\rm Xe}$ vs the Coulomb V_H. Columns 4 and 5 give the deviation in position and height, respectively, of the peaks from Figs. 4(c) and 4(d).

Pattern	r_c (a.u.)	$V_{\rm Xe}(r_c)/V_H(r_c)$	angle dev	peak dev
Spiral	2.9	1.58	4.5°	0.66
Spider	6.0	1.06	1.7°	1.11

electron's closest distance to the core is roughly twice as large for the spider than the spiral (see Table II). At the tunnel exit, the photoelectrons will be too far from the core to differentiate V_H or $V_{\rm Xe}$. However, the close return of the spiral trajectories makes them sensitive to the structural information encoded in the effective potential. In Figs. 4(c) and 4(d), we compare the spiral and the spider directly by plotting the photoelectron signal as a function of the emission angle for a fixed energy $E = 9.5$ eV. The maximum deviations in position and height of the peaks, given in Table II, are much greater for the spiral. This confirms a much stronger sensitivity to the target via structural phases.

The strong sensitivity to changes in the Coulomb potential *after* ionization of the spiral-like interference pattern means this is the most promising interference pattern candidate for performing dynamic imaging. Tracking the peaks of the interference carpet away from $\theta = 90°$, which shift and distorted with differences in the potential, allows information about the residual binding potential to be collected. A future prospect could be to fit experimental data with results from the CQSFA or a TDSE model incorporating changes to a model potential, which could be used to "image" and track the dynamics of the potential. By employing a pump probe scheme or tailored fields, the delay between fields could be varied, effectively time stamping the data and helping to reconstruct dynamics.

C. Alternative targets and comparison with ab initio methods

In Fig. 5, we compare CQSFA [Figs. 5(a) and 5(c)] and TDSE [Figs. 5(b) and 5(d)] calculations for helium and neon. In the TDSE computations, a four-cycle a trapezoidal pulse envelope was used with a four-cycle constant top. We have verified that by changing the pulse length the ATI peaks become much sharper, but the position of the interference structures is not affected (not shown).

The spiral-like fringes are visible in the highest energy region near $\theta = 90°$, but are less prominent than for xenon. This demonstrates that the spiral-like interference is not limited to xenon or those particular laser parameters. As before, lines have been placed on the figures to trace the spiral fringes. The lines are shifted by a single photon energy ($\approx$1.55 eV) between helium and neon. This is due to orbits 3 and 4 leaving from opposite sides of the atom, and the valence orbitals of helium and neon having opposite (even and odd, respectively) parities. This leads to the two sets of fringes being out of phase. Note that the fringes between the CQSFA and QPROP calculation are shifted but crucially both models show out-of-phase fringes between targets. Comparing two

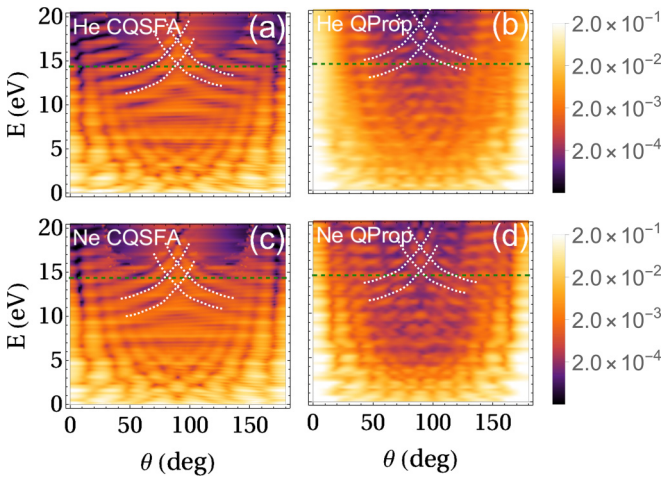

FIG. 5. CQSFA (left) and time-dependent Schrödinger equation (TDSE) computations performed with QProp [59] (right) for helium (top) and neon (bottom) for the same frequency and number of cycles as Fig. 2 with an intensity $I = 1.2 \times 10^{14}$ W/cm^2. The TDSE computations have been performed for an trapezoidal pulse with a four-cycle flat top. The results have been focally averaged [52]. The $2U_p$ cutoff is marked by a green dashed line. The spiral-like fringes are traced by dotted white lines.

targets, such as N_2 and neon in Ref. [46], allows the spiral to be exploited as a sensitive probe of orbital parity. It should be noted that recently it has been shown in Ref. [44] that the window operator, employed in these QPROP computations, can lead to aberrations and overestimation close to $\theta = 90°$.

IV. CONCLUSIONS

In conclusion, we have found a holographic spiral-like structure first predicted in Ref. [33], both in experiment and theory, and have identified it as the cause of interference carpets. We find that the 2ω gap in the interference carpets is a universal feature inherent to the field symmetry, which can be satisfied by many pairs of trajectories across different models for ATI.

The spiral has been overlooked until now, for the following reasons. First, the original explanations for the interference carpets [23,24,28,29] were based on the direct SFA. Second, there was lack of proper theoretical treatment of a wide range of orbits considered by the CQSFA, for which both the potential *and* the field are equally important. In particular, the Couloumb-distorted orbits 3 and 4 do not exist in any SFA models, and their interference has only been described using the CQSFA. Thus, the prospects of the spiral for holographic imaging have not been realized.

Attributing the carpet interference to direct electron pathways has deterred any previous study into using it for holographic imaging. So far, interference carpets have solely been used for determining initial phases such as those stemming from bound-state parity. Yet, the spiral is ideal for holographic imaging due to its high sensitivity to structural Coulomb phases. Furthermore, in contrast to the fish-bone structure [17], it requires no further manipulation to be observed. Finally, the half-cycle separation between the pathways that form the spiral means that ultrafast dynamics could

be resolved. All this makes the spiral the ideal structure for imaging and photoelectron holography and we hope that this work can stimulate further research in this direction.

ACKNOWLEDGMENTS

This research was in part funded by the National Key Research and Development Program of China (No. 2019YFA0307702), the National Natural Science Foundation of China (No. 11834015, No. 11874392, and No. 11922413), the Strategic Priority Research Program of the Chinese Academy of Sciences (No. XDB21010400), and the UK Engineering and Physical Sciences Research Council (EPSRC) (Grants No. EP/J019143/1 and No. EP/P510270/1). The latter grant is within the remit of the InQuBATE Skills Hub for Quantum Systems Engineering. We thank the Wuhan Institute of Physics and Mathematics, Chinese Academy of Sciences, for its kind hospitality, and A. Staudte and H. Kang for useful discussions.

APPENDIX A: DERIVATION OF CARPET INTERFERENCE CONDITIONS

The Appendices complement the article by showing that carpet-like interference conditions are universal. In Appendix A, we show analytically that this holds for direct and rescattered ATI orbits in the strong-field approximation and for the CQSFA orbits. Our proof is exact for monochromatic linearly polarized fields, and a good approximation for sufficiently long pulses. Subsequently, in Appendix B, we provide examples that confirm the analytic conditions for angle $\theta = 90^\circ$ ($p_\parallel = 0$).

We demonstrate the universality of the carpet interference patterns for $p_\parallel = 0$, which are caused by the symmetry of the field. A linearly polarized monochromatic laser field will change sign every half-period $T/2$; i.e., the vector potential satisfies $\mathbf{A}(t) = -\mathbf{A}(t \pm T/2)$. Hence, there is symmetry for time translations $t \to t + T/2$ combined with a reflection $p_\parallel \to -p_\parallel$ of the momentum component in the direction of the laser-field polarization. In Refs. [23,24], this was discussed in the context of direct long and short orbits for the SFA. However, below we demonstrate that the carpet condition along $\theta = 90^\circ$ holds for the direct SFA (Appendix A 1), rescattered SFA (Appendix A 2), and the Coulomb quantum-orbit strong-field approximation (CQSFA) (Appendix A 3) for monochromatic linearly polarized fields.

1. Direct SFA

For the direct SFA, the action (with vector potential added explicitly) is

$$S(\mathbf{p}, t') = \left(I_p + U_p + \frac{1}{2}|\mathbf{p}|^2\right)t' + \frac{2\sqrt{U_p}p_\parallel}{\omega}\sin(\omega t') + \frac{U_p}{2\omega}\sin(2\omega t') \tag{A1}$$

and the saddle-point equation is

$$[\mathbf{p} + \mathbf{A}(t')]^2 = -2I_p, \tag{A2}$$

where t' denotes the ionization time, U_p is the ponderomotive energy, and I_p is the ionization potential. Let us assume that t_1' solves the saddle-point Eq. (A2) for the final momentum $\mathbf{p}_1$, and consider $t_2' = t_1' + T/2$ and $p_{2\parallel} = -p_{1\parallel}$. Inserting these into Eq. (A2) and considering the property upon $\mathbf{A}(t)$ above yields

$$\begin{aligned}[\mathbf{p}_2 + \mathbf{A}(t_2')]^2 &= [-p_{1\parallel} - A(t_1')]^2 + p_{1\perp}^2 \\ &= [\mathbf{p}_1 + \mathbf{A}(t_1')]^2 = -2I_p.\end{aligned} \tag{A3}$$

Thus, t_2' solves Eq. (A2) for $\mathbf{p}_2$. Now if $p_{1\parallel} = p_{2\parallel} = 0$, then $\mathbf{p}_1 = \mathbf{p}_2 = \mathbf{p}$ and the two solutions can interfere. Using the form given for the action by Eq. (A1), we can work out an interference condition

$$\begin{aligned}\Delta S_{12} &= S(\mathbf{p}, t_2') - S(\mathbf{p}, t_1') = 2\pi n \\ &= \left(I_p + U_p + \tfrac{1}{2}|\mathbf{p}|^2\right)T/2.\end{aligned} \tag{A4}$$

Substituing $T = 2\pi/\omega$, we obtain

$$\left(I_p + U_p + \tfrac{1}{2}p_\perp^2\right) = 2\omega n, \tag{A5}$$

which is the carpet condition as stated in Refs. [23,24].

2. Rescattered SFA

For rescattered ATI [53], the action (with vector potential added explicitly) is

$$\begin{aligned}S(\mathbf{p}, k, t'', t') = (I_p + U_p)t' - \frac{1}{2}k^2(t'' - t') + \frac{1}{2}\mathbf{p}^2 t'' \\ - \frac{2\sqrt{U_p}k}{\omega}[\sin(\omega t'') - \sin(\omega t')] \\ + \frac{2\sqrt{U_p}p_\parallel}{\omega}\sin(\omega t'') + \frac{U_p}{2\omega}\sin(2\omega t'),\end{aligned} \tag{A6}$$

where t' and t'' give the ionization and rescattering times, respectively, and k gives the intermediate electron momentum. The saddle-point equations are

$$[k + A(t')]^2 = -2I_p, \tag{A7}$$

$$[k + A(t'')]^2 = [\mathbf{p} + \mathbf{A}(t'')]^2, \tag{A8}$$

$$k = -\frac{1}{t'' - t'}\int_{t'}^{t''} A(\tau)d\tau. \tag{A9}$$

We now assume that parameters t_1', t_1'', and k_1 solve saddle-point Eqs. (A7)–(A9) for a final momentum $\mathbf{p}_1$. Then we let the following variables have the relation $t_2' = t_1' + T/2$, $t_2'' = t_1'' + T/2$, and $k_2 = -k_1$, while the final momentum $p_{2\parallel} = -p_{1\parallel}$. We will now show that this set of variables also solves Eqs. (A7)–(A9).

$$\begin{aligned}[k_2 + A(t_2')]^2 &= [-k_1 - A(t_1')]^2 \\ &= -2I_p.\end{aligned}$$

For the second saddle-point equation

$$\begin{aligned}[k_2 + A(t_2'')]^2 &= [-k_1 - A(t_1'')]^2 \\ &= [\mathbf{p}_1 + \mathbf{A}(t_1'')]^2 \\ &= [-p_{2\parallel} - A(t_2'')]^2 + p_\perp^2 \\ &= [\mathbf{p}_2 + \mathbf{A}(t_2'')]^2.\end{aligned}$$

Finally, for the third,

$$k_2 = -k_1 = \frac{1}{t_1'' - t_1'}\int_{t_1'}^{t_1''} A(\tau)d\tau$$
$$= \frac{1}{t_2'' - t_2'}\int_{t_2'-T/2}^{t_2''-T/2} A(\tau)d\tau$$
$$= -\frac{1}{t_2'' - t_2'}\int_{t_2'}^{t_2''} A(\tau)d\tau.$$

Thus, variables t_2', t_2'', and k_2 solve Eqs. (A7)–(A9) for a final momentum $\mathbf{p}_2$. As before, when $p_{1\parallel} = p_{2\parallel} = 0$, $\mathbf{p}_1 = \mathbf{p}_2 = \mathbf{p}$ and these two solutions can interfere. As in the previous case, we can compute the interference fringe condition,

$$\Delta S_{12} = S(\mathbf{p}, k_2, t_2'', t_2') - S(\mathbf{p}, k_1, t_1'', t_1') = 2\pi n$$
$$= \left(I_p + U_p + \tfrac{1}{2}|\mathbf{p}|^2\right)T/2, \tag{A10}$$

which leaves the carpet condition

$$\left(I_p + U_p + \tfrac{1}{2}p_\perp^2\right) = 2\omega n, \tag{A11}$$

as before. Thus, the carpet condition at $\theta = 90^\circ$ is as universal as ATI rings and appears in both rescattered and direct ATI. However, both of these fail to replicate the experiment, while CQSFA succeeds. In the following section, we will show that a similar condition can be derived for the CQSFA.

3. Coulomb-quantum orbit strong-field approximation

To proceed again, we need the action and saddle-point equations. The CQSFA action [19,34] reads

$$S(\mathbf{p}, \mathbf{r}, t, t') = (I_p + U_p)t' + \frac{1}{2}\mathbf{p}_f^2 t_r' + \frac{i}{2}\mathbf{p}_0^2 t_i' + \frac{U_p}{2\omega}\sin(2\omega t')$$
$$+ \frac{2\sqrt{U_p}}{\omega}[p_{0\parallel}\sin(\omega t') - (p_{0\parallel} - p_{f\parallel})\sin(\omega t_r')]$$
$$- \int_{t'}^{t_r'} V(\mathbf{r}_0(\tau))d\tau - \frac{1}{2}\int_{t_r'}^{t} \boldsymbol{\mathscr{P}}(\tau)\cdot[\boldsymbol{\mathscr{P}}(\tau)$$
$$+ 2\mathbf{p}_f + 2\mathbf{A}(\tau)]d\tau - 2\int_{t_r'}^{t} V(\mathbf{r}(\tau))d\tau, \tag{A12}$$

where $\mathbf{p}_0 = \mathbf{p}(t')$, $\mathbf{p}_f = \mathbf{p}(t)$, where t' and t denote the ionization and detection times, respectively,

$$\mathbf{r}_0(\tau) = \int_{t'}^{\tau}[\mathbf{p}_0 + \mathbf{A}(\tau')]d\tau' \tag{A13}$$

is the tunnel trajectory, and $\mathbf{p}(\tau) = \boldsymbol{\mathscr{P}}(\tau) + \mathbf{p}_f$. In Eq. (A12), $t_r' = \mathrm{Re}[t']$ and $t_i' = \mathrm{Im}[t']$. This has been chosen so that all the integrands go to zero for large τ. The saddle-point equations are given by

$$[\mathbf{p}(t') + \mathbf{A}(t')]^2 = -2I_p \tag{A14}$$

$$\dot{\mathbf{p}}(\tau) = -\nabla V(\mathbf{r}(\tau)) \tag{A15}$$

and

$$\dot{\mathbf{r}}(\tau) = \mathbf{p}(\tau) + \mathbf{A}(\tau). \tag{A16}$$

As before, let t_1', $\mathbf{p}_1(\tau)$, and $\mathbf{r}_1(\tau)$ solve Eqs. (A14)–(A17) for a final momentum $\mathbf{p}_{1f}$. For clarity, let us define the reflection matrix

$$\sigma_\parallel = \begin{pmatrix} -1 & 0 \\ 0 & 1 \end{pmatrix}, \tag{A17}$$

given in two dimensions, but the proof will hold for three dimensions as well. Then let $t_2' = t_1' + T/2$, $\mathbf{p}_2(\tau) = \sigma_\parallel \mathbf{p}_1(\tau - T/2))$, and $\mathbf{r}_2(\tau) = \sigma_\parallel \mathbf{r}_{1\perp}(\tau - T/2)$. Again, we can show these satisfy Eqs. (A14)–(A17) for a final momentum $\mathbf{p}_{2f} = (-p_{1f\parallel}, \mathbf{p}_{1f\perp})$.

The saddle-point equation (A14) then reads

$$[\mathbf{p}_2(t_2') + \mathbf{A}(t_2')]^2 = [-p_{1\parallel}(t_1') - A(t_1')]^2 + p_{1\perp}^2$$
$$= [\mathbf{p}_1(t_2') + \mathbf{A}(t_1')]^2$$
$$= -2I_p. \tag{A18}$$

Inserting $\mathbf{p}_2(\tau)$ into the left-hand side of Eq. (A15) gives

$$\dot{\mathbf{p}}_2(\tau) = \sigma_\parallel \mathbf{p}_1(\tau - T/2)$$
$$= -\sigma_\parallel \nabla V(\mathbf{r}_1(\tau - T/2)).$$

Bringing the reflection matrix inside the argument of the potential then yields

$$\dot{\mathbf{p}}_2(\tau) = -\nabla V(\sigma_\parallel \mathbf{r}_1(\tau - T/2))$$
$$= -\nabla V(\mathbf{r}_2(\tau)). \tag{A19}$$

Finally, one can also show that Eq. (A17) gives

$$\dot{\mathbf{r}}_2(\tau) = \sigma_\parallel(\mathbf{p}_1(\tau - T/2) + \mathbf{A}(\tau - T/2))$$
$$= \mathbf{p}_2(\tau) - \sigma_\parallel \mathbf{A}(\tau)$$
$$= \mathbf{p}_2(\tau) + \mathbf{A}(\tau). \tag{A20}$$

Thus t_2', $\mathbf{p}_2(\tau)$ and $\mathbf{r}_2(\tau)$ solve the saddle-point Eqs. (A14)–(A17) for a final momentum $\mathbf{p}_{2f}$. As before, if $p_{1f\parallel} = p_{2f\parallel} = 0$, then $\mathbf{p}_{1f} = \mathbf{p}_{2f}$ and these two solutions can interfere. The difference in their action is given by

$$\Delta S_{12} = S(\mathbf{p}_2, \mathbf{r}_2, t, t_2') - S(\mathbf{p}_1, \mathbf{r}_1, t, t_1') = 2\pi n$$
$$= \left(I_p + U_p + \tfrac{1}{2}|\mathbf{p}_f|^2\right)T/2 + \Delta I,$$

where ΔI are all the integral terms. Very similar cancellations can be made as the HATI case, leaving

$$\left(I_p + U_p + \tfrac{1}{2}\mathbf{p}_f^2\right) = 2n\omega - \frac{\omega}{\pi}\Delta I. \tag{A21}$$

In order to recover the carpet condition, we must show the integral terms also cancel or go to 0. We split this into three parts, $\Delta I = \Delta I_{V_1} + \Delta I_p + \Delta I_{V_2}$, which correspond to the terms as they appear in order in the action given in Eq. (A12):

$$\Delta I_{V_1} = \int_{t_1'+T/2}^{t_{1r}'+T/2} V([\sigma_\parallel \mathbf{r}_{10}(\tau - T/2)])d\tau - \int_{t'}^{t_{1r}'} V(\mathbf{r}_{10}(\tau))d\tau,$$

where that $r_{10}(\tau)$ is given by Eq. (A13). If the first integral is transformed by $\tilde{\tau} \to \tau - T/2$, then the two integrals become the same besides the reflection matrix $\sigma_\parallel$ in the argument of the potential of the first integral. As the potential takes the square of $\mathbf{r}$, the reflection matrix is applied twice, which gives

the identity and both terms cancel. Hence, $\Delta I_{V_1} = 0$, and

$$\begin{aligned}\Delta I_p = &-\frac{1}{2}\int_{t'_{1r}+T/2}^{t} \sigma_\parallel \boldsymbol{\mathscr{P}}_1(\tau - T/2)\cdot[\sigma_\parallel \boldsymbol{\mathscr{P}}_1(\tau) \\ &+ 2\sigma_\parallel \mathbf{p}_f + 2\sigma_\parallel \mathbf{A}(\tau - T/2)]d\tau \\ &+\frac{1}{2}\int_{t'_{1r}}^{t} \boldsymbol{\mathscr{P}}_1(\tau)\cdot[\boldsymbol{\mathscr{P}}_1(\tau) + 2\mathbf{p}_f + 2\mathbf{A}(\tau)]d\tau.\end{aligned}$$

The $\sigma_\parallel$ matrices will multiply through to identity matrices. Then the same transformation $\tilde{\tau} \to \tau - T/2$ can be made as for I_{V_1}, which simplifies to

$$\begin{aligned}\Delta I_p &= -\frac{1}{2}\int_{t'_{1r}}^{t-T/2} \boldsymbol{\mathscr{P}}_1(\tau)\cdot[\boldsymbol{\mathscr{P}}_1(\tau) + 2\mathbf{p}_f + 2\mathbf{A}(\tau)]d\tau \\ &+\frac{1}{2}\int_{t'_{1r}}^{t} \boldsymbol{\mathscr{P}}_1(\tau)\cdot[\boldsymbol{\mathscr{P}}_1(\tau) + 2\mathbf{p}_f + 2\mathbf{A}(\tau)]d\tau \\ &= \frac{1}{2}\int_{t-T/2}^{t} \boldsymbol{\mathscr{P}}_1(\tau)\cdot[\boldsymbol{\mathscr{P}}_1(\tau) + 2\mathbf{p}_f + 2\mathbf{A}(\tau)]d\tau,\end{aligned} \tag{A22}$$

which is a single integral over the interval $(t - T/2, t)$. Given $\boldsymbol{\mathscr{P}}_1(t) \to 0$ as $t \to \infty$, then $\Delta I_p \to 0$ as $t \to \infty$. For the final integrals, a similar logic is used:

$$\Delta I_{V_2} = -2\int_{t'_{1r}+T/2}^{t} V(\sigma_\parallel \mathbf{r}_1(\tau - T/2))d\tau + 2\int_{t'_{1r}}^{t} V(\mathbf{r}_1(\tau))d\tau.$$

Using the same simplifications and transformation as above, we find

$$\Delta I_{V_2} = 2\int_{t}^{t-T/2} V(\mathbf{r}_1(\tau))d\tau. \tag{A23}$$

As before $V(\mathbf{r}_1(t)) \to 0$ as $t \to \infty$; hence $\Delta I_{V_1} \to 0$ as $t \to \infty$. Thus, in the limit as $t \to \infty$, $\Delta I \to 0$ and we recover the carpet interference pattern. This, together with the previous proofs, shows that the carpet condition is not unique to direct ATI.

APPENDIX B: CARPET PLOTS

In this section, we provide examples that confirm the validity of the carpet condition derived above. In Fig. 6, we plot the photoelectron spectra along $\theta = 90°$. Here we show signal from the pairs of orbits in different models that give rise to the carpet condition. The direct SFA spectrum was computed using long and short orbits, the CQSFA computation incorporates the orbits that lead to the fan and the spiral (i.e., orbits 1 and 2, and orbits 3 and 4, respectively) and the HATI spectrum considers two orbits separated by a half-cycle. All models give clear regularly spaced 2ω gaps. However, the minima and maxima occur in different places for each model; thus they will not all be appropriate for replication or analysis of experimental results. In Fig. 7, we plot the photoelectron

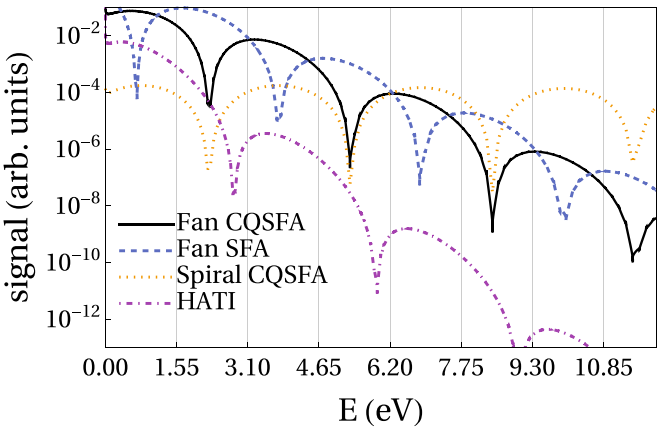

FIG. 6. ATI spectra for xenon at a fixed emission angle of $\theta = 90°$ for a peak laser intensity of $7 \times 10^{13}\,\mathrm{W/cm^2}$ over a single laser cycle for different approaches. The remaining parameters are the same as Fig. 2. The vertical grid marks intervals of $\omega = 1.55\,\mathrm{eV}$.

probability distributions over energy and θ for the same pairs of orbits. The spiral-like interference is radically different from the direct CQSFA and SFA pairs in Figs. 7(a) and 7(b), demonstrating that the Coulomb potential is crucial. The fact that the HATI results in Fig. 7(d) do not reflect the spiral suggests that this interference pattern is present only in models that account for Coulomb distortion of electron trajectories. Thus, we have demonstrated analytically and numerically that the carpet condition universally holds for many ATI physical mechanisms and models, due to a symmetry of the driving field. However, despite this, there are large qualitative differences between the resulting interference fringes and thus care should be employed when using these fringes to interpret experimental results.

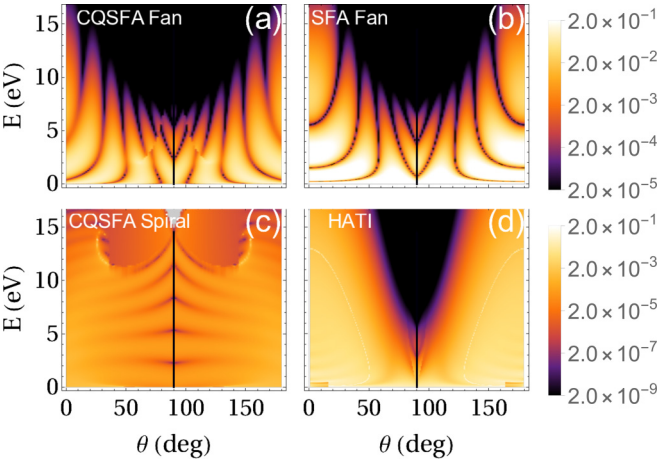

FIG. 7. Energy vs θ density plots for pairs of orbits that can lead to carpet-like distributions. The same field and target parameters and labeling convention has been used as Fig. 6. The black vertical line in each panel corresponds to $\theta = 90°$, for which the cross section in Fig. 6 were computed. Note these have not been focally averaged and are plotted over log scale. Each plot is normalized by the peak value.

[1] P. Salières, A. Maquet, S. Haessler, J. Caillat, and R. Taïeb, Rep. Prog. Phys. **75**, 062401 (2012).

[2] F. Lépine, M. Y. Ivanov, and M. J. J. Vrakking, Nat. Photon. **8**, 195 (2014).

[3] S. R. Leone, C. W. McCurdy, J. Burgdörfer, L. S. Cederbaum, Z. Chang, N. Dudovich, J. Feist, C. H. Greene, M. Ivanov, R. Kienberger, U. Keller, M. F. Kling, Z.-H. Loh, T. Pfeifer, A. N. Pfeiffer, R. Santra, K. Schafer, A. Stolow, U. Thumm, and M. J. J. Vrakking, Nat. Photon. **8**, 162 (2014).

[4] E. Lindroth, F. Calegari, L. Young, M. Harmand, N. Dudovich, N. Berrah, and O. Smirnova, Nat. Rev. Phys. **1**, 107 (2019).

[5] F. Calegari, D. Ayuso, A. Trabattoni, L. Belshaw, S. De Camillis, S. Anumula, F. Frassetto, L. Poletto, A. Palacios, P. Decleva, J. B. Greenwood, F. Martín, and M. Nisoli, Science **346**, 336 (2014).

[6] F. Calegari, G. Sansone, S. Stagira, C. Vozzi, and M. Nisoli, J. Phys. B **49**, 062001 (2016).

[7] D. Ayuso, O. Neufeld, A. F. Ordonez, P. Decleva, G. Lerner, O. Cohen, M. Ivanov, and O. Smirnova, Nat. Photon. **13**, 866 (2019).

[8] S. Rozen, A. Comby, E. Bloch, S. Beauvarlet, D. Descamps, B. Fabre, S. Petit, V. Blanchet, B. Pons, N. Dudovich, and Y. Mairesse, Phys. Rev. X **9**, 031004 (2019).

[9] J. E. Bækhøj, C. Lévêque, and L. B. Madsen, Phys. Rev. Lett. **121**, 023203 (2018).

[10] M. Spanner, O. Smirnova, and P. B. Corkum, J. Phys. B **37**, L243 (2004).

[11] X. B. Bian, Y. Huismans, O. Smirnova, K. J. Yuan, M. J. J. Vrakking, and A. D. Bandrauk, Phys. Rev. A **84**, 043420 (2011).

[12] Y. Huismans, A. Rouzée, A. Gijsbertsen, J. H. Jungmann, A. S. Smolkowska, P. S. W. M. Logman, F. Lépine, C. Cauchy, S. Zamith, T. Marchenko, J. M. Bakker, G. Berden, B. Redlich, A. F. G. Van Der Meer, H. G. Muller, W. Vermin, K. J. Schafer, M. Spanner, M. Y. Ivanov, O. Smirnova *et al.*, Science **331**, 61 (2011).

[13] C. F. de Morisson Faria and A. S. Maxwell, Rep. Prog. Phys. **83**, 034401 (2020).

[14] D. D. Hickstein, P. Ranitovic, S. Witte, X.-M. Tong, Y. Huismans, P. Arpin, X. Zhou, K. E. Keister, C. W. Hogle, B. Zhang, C. Ding, P. Johnsson, N. Toshima, M. J. J. Vrakking, M. M. Murnane, and H. C. Kapteyn, Phys. Rev. Lett. **109**, 073004 (2012).

[15] A. Rudenko, K. Zrost, C. D. Schröter, V. L. B. de Jesus, B. Feuerstein, R. Moshammer, and J. Ullrich, J. Phys. B **37**, L407 (2004).

[16] C. M. Maharjan, A. S. Alnaser, I. Litvinyuk, P. Ranitovic, and C. L. Cocke, J. Phys. B **39**, 1955 (2006).

[17] M. Haertelt, X. B. Bian, M. Spanner, A. Staudte, and P. B. Corkum, Phys. Rev. Lett. **116**, 133001 (2016).

[18] X. Y. Lai, S. G. Yu, Y. Y. Huang, L. Q. Hua, C. Gong, W. Quan, C. F. d. M. Faria, and X. J. Liu, Phys. Rev. A **96**, 013414 (2017).

[19] A. S. Maxwell, A. Al-Jawahiry, T. Das, and C. Figueira de Morisson Faria, Phys. Rev. A **96**, 023420 (2017).

[20] Y. Mi, N. Camus, L. Fechner, M. Laux, R. Moshammer, and T. Pfeifer, Phys. Rev. Lett. **118**, 183201 (2017).

[21] M. Meckel, A. Staudte, S. Patchkovskii, D. M. Villeneuve, P. B. Corkum, R. Dörner, and M. Spanner, Nat. Phys. **10**, 594 (2014).

[22] S. Walt, R. Bhargava, M. Atala, N. I. Shvetsov-Shilovski, A. von Conta, D. Baykusheva, M. Lein, and H. Wörner, Nat. Commun. **8**, 15651 (2017).

[23] P. A. Korneev, S. V. Popruzhenko, S. P. Goreslavski, W. Becker, G. G. Paulus, B. Fetić, and D. B. Milošević, New J. Phys. **14**, 055019 (2012).

[24] P. A. Korneev, S. V. Popruzhenko, S. P. Goreslavski, T. M. Yan, D. Bauer, W. Becker, M. Kübel, M. F. Kling, C. Rödel, M. Wünsche, and G. G. Paulus, Phys. Rev. Lett. **108**, 223601 (2012).

[25] W. Becker and M. Kleber, Phys. Scr. **94**, 023001 (2019).

[26] P. Kazemi, S. Chaturvedi, I. Marzoli, R. F. O'Connell, and W. P. Schleich, New J. Phys. **15**, 013052 (2013).

[27] M. Li, J. W. Geng, M. M. Liu, X. Zheng, L. Y. Peng, Q. Gong, and Y. Liu, Phys. Rev. A **92**, 013416 (2015).

[28] M. A. Almajid, M. Zabel, S. Skruszewicz, J. Tiggesbaumker, and D. Bauer, J. Phys. B **50**, 194001 (2017).

[29] L. Guo, S. S. Han, S. L. Hu, and J. Chen, J. Phys. B **50**, 125006 (2017).

[30] X. Ren and J. Zhang, Optik **181**, 287 (2019).

[31] M. Li, J. W. Geng, H. Liu, Y. Deng, C. Wu, L. Y. Peng, Q. Gong, and Y. Liu, Phys. Rev. Lett. **112**, 113002 (2014).

[32] W. Becker, S. P. Goreslavski, D. B. Milošević, and G. G. Paulus, J. Phys. B **51**, 162002 (2018).

[33] A. S. Maxwell and C. Figueira de Morisson Faria, J. Phys. B **51**, 124001 (2018).

[34] X. Y. Lai, C. Poli, H. Schomerus, and C. F. d. M. Faria, Phys. Rev. A **92**, 043407 (2015).

[35] A. S. Maxwell, A. Al-Jawahiry, X. Y. Lai, and C. Figueira de Morisson Faria, J. Phys. B **51**, 044004 (2018).

[36] W. Becker, F. Grasbon, R. Kopold, D. B. Milošević, G. G. Paulus, and H. Walther, Adv. At. Mol. Opt. Phys. **48**, 35 (2002).

[37] A. S. Maxwell, S. V. Popruzhenko, and C. Figueira de Morisson Faria, Phys. Rev. A **98**, 063423 (2018).

[38] S. V. Popruzhenko, J. Phys. B **47**, 204001 (2014).

[39] S. V. Popruzhenko, V. D. Mur, V. S. Popov, and D. Bauer, J. Exp.: Theor. Phys. **108**, 947 (2009).

[40] M. F. Guest, I. J. Bush, H. J. Van Dam, P. Sherwood, J. M. Thomas, J. H. Van Lenthe, R. W. Havenith, and J. Kendrick, Mol. Phys. **103**, 719 (2005).

[41] X. Liu and C. Figueira de Morisson Faria, Phys. Rev. Lett. **92**, 133006 (2004).

[42] X. Xie, T. Wang, S. G. Yu, X. Y. Lai, S. Roither, D. Kartashov, A. Baltuška, X. J. Liu, A. Staudte, and M. Kitzler, Phys. Rev. Lett. **119**, 243201 (2017).

[43] W. Quan, X. Y. Lai, Y. J. Chen, C. L. Wang, Z. L. Hu, X. J. Liu, X. L. Hao, J. Chen, E. Hasović, M. Busuladžić, W. Becker, and D. B. Milošević, Phys. Rev. A **88**, 021401(R) (2013).

[44] B. Fetić, W. Becker, and D. B. Milošević, Phys. Rev. A **102**, 023101 (2020).

[45] L. B. Madsen, L. A. A. Nikolopoulos, T. K. Kjeldsen, and J. Fernández, Phys. Rev. A **76**, 063407 (2007).

[46] H. P. Kang, A. S. Maxwell, D. Trabert, X. Y. Lai, S. Eckart, M. Kunitski, M. Schöffler, T. Jahnke, X. B. Bian, R. Dörner, and C. Figueira de Morisson Faria, Phys. Rev. A **102**, 013109 (2020).

[47] D. B. Milošević, W. Becker, M. Okunishi, G. Prümper, K. Shimada, and K. Ueda, J. Phys. B **43**, 015401 (2010).

[48] X. M. Tong and C. D. Lin, J. Phys. B **38**, 2593 (2005).
[49] T. M. Yan, S. V. Popruzhenko, M. J. J. Vrakking, and D. Bauer, Phys. Rev. Lett. **105**, 253002 (2010).
[50] A. T. Eppink and D. H. Parker, Rev. Sci. Instrum. **68**, 3477 (1997).
[51] V. Dribinski, A. Ossadtchi, V. A. Mandelshtam, and H. Reisler, Rev. Sci. Instrum. **73**, 2634 (2002).
[52] R. Kopold, W. Becker, M. Kleber, and G. G. Paulus, J. Phys. B **35**, 217 (2002).
[53] A. Lohr, M. Kleber, R. Kopold, and W. Becker, Phys. Rev. A **55**, R4003(R) (1997).
[54] M. D. Śpiewanowski and L. B. Madsen, Phys. Rev. A **91**, 043406 (2015).
[55] C. Figueira de Morisson Faria, H. Schomerus, and W. Becker, Phys. Rev. A **66**, 043413 (2002).
[56] W. Becker and D. B. Milošević, J. Phys. B **48**, 151001 (2015).
[57] M. Möller, F. Meyer, A. M. Sayler, G. G. Paulus, M. F. Kling, B. E. Schmidt, W. Becker, and D. B. Milošević, Phys. Rev. A **90**, 023412 (2014).
[58] W. Becker and D. B. Milošević, J. Phys.: Conf. Ser. **691**, 012002 (2016).
[59] D. Bauer and P. Koval, Comput. Phys. Commun. **174**, 396 (2006).